J. Space Weather Space Clim. 2022, **12**, 40
© Y. Zheng et al., Published by EDP Sciences 2022
https://doi.org/10.1051/swsc/2022036

JSWSC

Available online at:
www.swsc-journal.org

Topical Issue - Ionospheric plasma irregularities and their impact on radio systems

RESEARCH ARTICLE OPEN ACCESS

The refractive and diffractive contributions to GPS signal scintillation at high latitudes during the geomagnetic storm on 7–8 September 2017

Yuhao Zheng[1], Chao Xiong[1,2,*], Yaqi Jin[3], Dun Liu[4], Kjellmar Oksavik[5,6], Chunyu Xu[1], Yixun Zhu[1], Shunzu Gao[1], Fengjue Wang[1], Hui Wang[1], and Fan Yin[1]

[1] Department of Space Physics, Electronic Information School, Wuhan University, 430072 Wuhan, China
[2] Hubei Luojia Laboratory, 430079 Wuhan, China
[3] Department of Physics, University of Oslo, PO Box 1048, Blindern, 0316 Oslo, Norway
[4] No. 22nd Research Institute, CETC, 266107 Qingdao, Shandong, China
[5] Birkeland Centre for Space Science, Department of Physics and Technology, University of Bergen, PO Box 7803, 5020 Bergen, Norway
[6] University Centre in Svalbard, N-9171 Longyearbyen, Norway

Received 15 June 2022 / Accepted 24 October 2022

Abstract—Different indices have been used to reflect, or monitor the ionospheric scintillation, e.g. the detrended carrier phase, σ_φ, S_4, the rate of change of the vertical total electron content index (νROTI), as well as the ionosphere-free linear combination (IFLC) of two carrier phases. However, few studies have been performed to investigate the refractive and diffractive contributions to these indices, especially during geomagnetic storms. In this study, we analyze the high-resolution (50 Hz) phase and amplitude measurements from four high-latitude stations in Svalbard, Norway during the geomagnetic storm on 7–8 September 2017. Our results show that at high latitudes, the high-pass filter with a standard cutoff frequency of 0.1 Hz sometimes cannot effectively remove the refraction-driven phase variations, especially during the geomagnetic storm, leading to a remaining refraction contribution to the detrended carrier phase and σ_φ when scintillation happens. In the meanwhile, as νROTI is sensitive to the TEC gradients, regardless of small- or large-scale ionospheric structures, both refraction and diffraction effects can cause visible fluctuations of νROTI. For most of the scintillation events, the phase indices (including detrended carrier phase, σ_φ, and νROTI), IFLC, and S_4 show consistent fluctuations, indicating that diffraction usually occurs simultaneously with refraction during scintillation. One interesting feature is that although the IFLC and S_4 are thought to be both related to the diffraction effect, they do not always show simultaneous correspondence during scintillations. The IFLC is enhanced during the geomagnetic storm, while such a feature is not seen in S_4. We suggest that the enhanced IFLC during the geomagnetic storm is caused by the increased high-frequency phase power, which should be related to the enhanced density of small-scale irregularities during storm periods.

Keywords: Refraction / Diffraction / Plasma irregularity / Scintillation / Geomagnetic storm

1 Introduction

When propagating through the ionosphere, radio waves interact with the free electrons, resulting in signal group delay and phase advance (Kintner et al., 2007). If small-scale plasma irregularities exist in the propagation path, radio waves received by ground receivers usually show rapid fluctuations in both phase and amplitude, referred to as ionospheric scintillation (e.g., Kintner et al., 2007). With the development of the Global Navigation Satellite System (GNSS) in past decades, ionospheric scintillations at L-band frequencies have been widely studied (e.g., Basu et al., 1980; Aarons, 1982; Aarons & Basu, 1994; Kintner et al., 2007). From a global perspective, ionospheric scintillation is most prominent at equatorial and low latitudes, as well as in polar regions.

The scintillation of GNSS signals is generally classified into refraction and diffraction effects. The refraction of the signal phase is determinative, which is related to the wave frequency and electron density along the propagation path, while the diffraction is stochastic and independent of the wave frequency

*Corresponding author: xiongchao@whu.edu.cn

(Carrano et al., 2013). One important factor that causes refraction or diffraction, or both of them, is the size of plasma irregularities that the radio wave strikes (e.g., Yeh & Liu, 1982). Refraction occurs for plasma density structures at all scale sizes, while for diffraction the plasma density structure, or irregularity, must be equal to or smaller than the Fresnel scale (e.g., Bittencourt, 2004; Kintner et al., 2007). The Fresnel scale is approximately defined as $r_f = \sqrt{2\lambda z}$, where λ is the wavelength of the signal and z is the height of the irregularity layer above the receiver. Here the approximation is valid only when the distance between the transmitter and receiver is much larger than the value of z. Ionospheric irregularities of these scale sizes cause diffractive variation of amplitude at the Fresnel frequency $f_F = \frac{v_d}{r_f}$ and greater, where v_d is the drift velocity of the plasma irregularity with respect to the ionospheric pierce point of the radio wave (Rino & Fremouw, 1977). When diffraction occurs, phase fluctuation or phase scintillation is caused by both refraction and diffraction (Cordes et al., 1986). For the signal amplitude, the refraction may change the radio wave path and result in small decreases in wave power, due to reflection and absorption, but it will not cause obvious wave amplitude fluctuations (e.g., McCaffrey & Jayachandran, 2019). From this perspective, amplitude fluctuation, or amplitude scintillation is mainly caused by the diffraction effect.

A practical approach that has been widely used for modeling the ionospheric scintillation intensity at ground level is the phase screen approximation (e.g., Booker et al., 1950; Rino, 1979a, b). In the phase screen model, the plasma irregularity is confined to an infinitely thin layer, which aims to model the primary effect on radio wave propagation through Fresnel-scale plasma irregularities as a function of the integral of the permittivity fluctuations along the ray path. This phase screen approximation provides a good basis for the theory behind signal amplitude and phase scintillation, which has been validated by using ground-based GNSS observations (e.g., Aarons & Basu, 1994; Pi et al., 1997). Recent work has also simulated the phase and amplitude scintillations for GNSS receivers onboard Low Earth orbiting (LEO) satellites (e.g., Xu et al., 2018), by using a two-component power-law phase screen model proposed by Carrano & Rino (2016). Xiong et al. (2020) compared the spaceborne GNSS observations from LEO satellites at different altitudes. They found that for receivers flying inside the ionospheric plasma irregularities, like the Swarm satellite at about 400–500 km altitude, only intense phase fluctuation and almost no amplitude degradation (less than 2 dB-Hz) were observed; while for lower-flying LEO satellites, like the Gravity Field and Steady-State Ocean Circulation Explorer (GOCE) satellite at about 250 km altitude, amplitude degradation of about 10 dB-Hz was often observed associated with intense phase fluctuation. This observational result confirms the phase screen model proposed by Rino (1979a, b) that within the thin layer of the phase screen, only radio wave phase changes; after the distorted radio wavefronts leave the phase screen layer and continue propagating, the received signal at lower altitude (e.g., ground) show noticeable amplitude fluctuations.

Different processes causing radio wave phase and amplitude fluctuations provide a possible way to separate the refraction and diffraction effects during ionospheric scintillation. As refraction mainly causes low-frequency phase variations, they were considered to be removable by a high-pass filter. van Dierendonck et al. (1993) suggested to use of a 6th-order Butterworth high-pass filter with a cutoff frequency of 0.1 Hz, and such a threshold works quite well for the GNSS data processing at the low and middle latitudes (e.g., van Dierendonck & Arbesser-Rastburg, 2004). However, at high latitudes, the plasma drift velocity is typically one or two orders of magnitude larger than the values at low and middle latitudes, thus the Fresnel frequency (proportional to the plasma drift velocity) often exceeds 0.1 Hz, leading to the known issue of "phase without amplitude scintillation at high latitude" (e.g., Forte & Radicella, 2002; Beach, 2006; Carrano & Rino, 2016; Wang et al., 2018; Ghobadi et al., 2020). With the standard cutoff frequency at 0.1 Hz applied to high-latitude GNSS data, sometimes the refractive phase variations still exist, which has often been wrongly treated as diffraction-driven scintillation (McCaffrey & Jayachandran, 2019). Although studies have tried high-pass filters with different cutoff frequencies (e.g., Forte, 2005; Mushini et al., 2012), no conclusive answer has been found so far for a cutoff frequency that can effectively eliminate the refraction-driven phase variations at high latitudes under all circumstances. Instead, McCaffrey & Jayachandran (2019) suggested that the ionosphere-free linear combination (IFLC) of phases on two carriers is an effective way to exclude the refraction-driven phase variations at high latitudes.

In addition to the detrended carrier phase and IFLC, other indices like σ_φ, S_4, and the rate of change of the total electron content index (ROTI) have also been widely used to monitor ionospheric scintillation. However, to our knowledge, there is no dedicated study that has investigated the relation between refraction/diffraction and these indices. As shown by McCaffrey & Jayachandran (2019), the remaining phase variations in the index IFLC are mainly non-refractive, it may be worthwhile to check the consistency between IFLC and signal amplitude scintillation, as both parameters are only attributed to the diffraction effect, as discussed above. Therefore, in this study, we provide a detailed survey to diagnose the refractive and diffractive contributions to these scintillation indices, by using the high-resolution GNSS measurements at high latitudes in the European Arctic during the geomagnetic storm on 7–8 September 2017. It also allows us to check if the contributions to these scintillation indices from the refraction and diffraction differ before and during the geomagnetic storm.

The structure of this study is arranged as below: in Section 2 the dataset and the definitions of scintillation indices are briefly introduced; observational results from the four GNSS receivers are presented in Section 3; discussion and comparison with previous studies are provided in Section 4; and the main findings are summarized in Section 5.

2 Dataset and approaches

2.1 Dataset

The data used in this study originates from four GNSS receivers referred to as Kjell Henriksen Observatory (KHO), Hopen (HOP), Ny-Ålesund (NYA), and Bjørnøya (BJN), located in Svalbard, Norway (Oksavik et al., 2015; Oksavik, 2020). They are the NovAtel GPStation-6 receivers operated by the University of Bergen, which can track signals from the

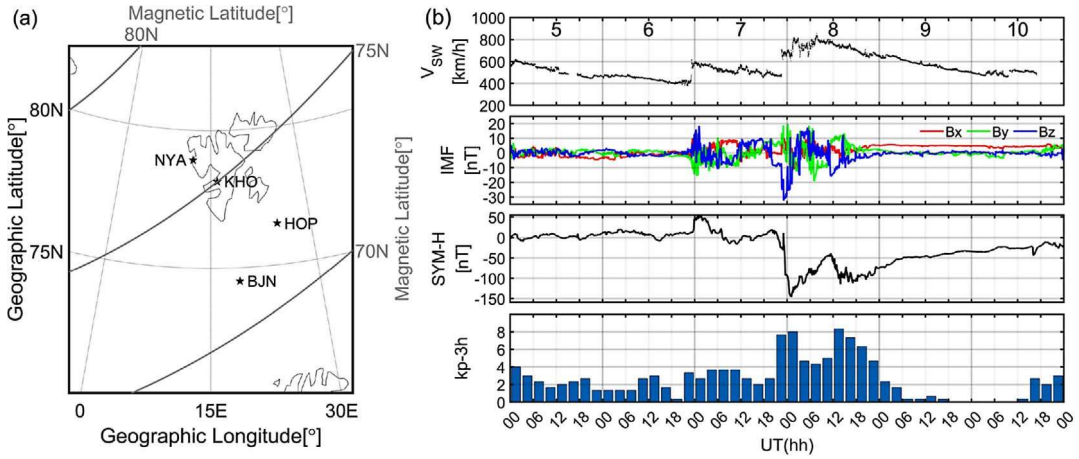

Figure 1. (a) The location of four GNSS stations in Svalbard, Norway used in this study. (b) Variations of V_{SW}, three components of IMF, SYM-H, and *Kp* indices during 5–10 September 2017.

Table 1. Geographical and geomagnetic coordinates of GPS stations.

	Geographic latitude	Geographic longitude	Magnetic latitude	Magnetic longitude
KHO	78.147° N	16.038° E	75.001° N	127.471° E
HOP	76.509° N	25.014° E	72.518° N	129.660° E
BJN	74.504° N	19.001° E	73.632° N	122.041° E
NYA	78.920° N	11.950° E	76.118° N	127.091° E

GPS, GLONASS, and GALILEO at different frequencies. All four receivers provide the phase and amplitude measurements with a time resolution of 50 Hz.

Figure 1a shows their location, covering the geographic latitudes of 72°–78° and geographic longitude of 0°–30° E. Their corresponding magnetic latitude and longitude are shown in Table 1. Here, we use the quasi-dipole model to calculate the magnetic coordinates (e.g., Emmert et al., 2010).

2.2 Ionospheric scintillation indices and definitions

The carrier phase measured at the ground contains usually diffraction and refraction effects, we, therefore, start with the basic equation for illustrating the different contributions to the carrier phase. Refraction is thought to occur when the GPS signal passes through the ionosphere, regardless of the ionospheric structure scale sizes. By ignoring the higher-order terms and path curvature, the phase delay caused by refraction is defined as (Kashcheyev et al., 2012):

$$I = \frac{40.308}{f^2}\int N_e \mathrm{d}s, \tag{1}$$

where f is the signal carrier frequency, N_e is the ionospheric electron density, ds is the ray path, and $\int N_e$ is the integrated electron density along the ray path that is referred to as the total electron content (TEC).

By assuming the propagation paths are the same at two different carrier frequencies, e.g., represented by i and j, the ratio between the two carrier phase delays satisfies:

$$\frac{I_i}{I_j} = \frac{f_j^2}{f_i^2}. \tag{2}$$

Considering the possible impact of receiver inaccuracies in the L2 carrier in monitoring the ionosphere (e.g., McCaffrey et al., 2018; Yasyukevich et al., 2021), GPS L1C/A and L5Q carriers were used in our study. For GPS L1 (1.575 GHz) and L5 (1.176 GHz) carriers, the theoretical ratio between the two carrier phase delay is 1.79.

Contributions to cause the carrier phase variations, at a constant frequency, can be generally divided into three parts:

$$L = r + \lambda N - I, \tag{3}$$

where r is the geometric distance between the GNSS satellite and the receiver, λ is the signal wavelength, N is the integer ambiguity, and I is the ionospheric delay part. The contributions from multipath, noise, and clock errors have been neglected. The geometric distance caused by carrier phase variation are low-frequency signals and the integer ambiguity is constant, therefore, in practice, they can be removed by a high-pass filter. Here we used the standard 6th-order Butterworth high-pass filter with a cutoff frequency of 0.1 Hz (van Dierendonck et al., 1993).

The IFLC of phases at two carrier frequencies f_i and f_j is then defined (Carrano et al., 2013):

$$\mathrm{IFLC}_{ij} = \frac{f_i^2 L_i - f_j^2 L_j}{f_i^2 - f_j^2} = r + \frac{f_i^2}{f_i^2 - f_j^2}\lambda_i N_i - \frac{f_j^2}{f_i^2 - f_j^2}\lambda_j N_j, \tag{4}$$

where the ionospheric delay part (I) has been removed. As shown in equation (1), the refraction-caused phase variation follows the inverse-frequency-squared relationship while the diffractive variation doesn't, the phase variations remaining in the IFLC are considered to be non-refractive and related

to the diffraction and other high- frequency disturbances (Carrano et al., 2013).

The amplitude scintillation is usually quantified by the S_4 index, which is derived from the detrended signal intensity. The signal intensity is actually the received signal power, measured in such a way that its value does not fluctuate with the noise power. Therefore, it cannot be represented by either the signal-to-noise ratio (SNR) or carrier-to-noise density (C/N0) (van Dierendonck et al., 1993). Here, the S_4 index is defined as the ratio of the standard deviation of the signal intensity to the mean signal intensity:

$$S_4 = \sqrt{\frac{\langle \mathrm{SI}^2 \rangle - \langle \mathrm{SI} \rangle^2}{\langle \mathrm{SI} \rangle^2}}, \tag{5}$$

where $\langle\ \rangle$ denotes the mathematical expectation within a certain period, e.g., 60 s. In practice, this time can be longer or shorter, but it must be longer than the Fresnel length divided by the irregularity drift velocity (Kintner et al., 2007). SI is the signal intensity (square of the amplitude) that is detrended via dividing the raw signal intensity SI_{raw} by the filtered signal intensity ($\mathrm{SI}_{\mathrm{filtered}}$) using a 6th-order Butterworth low-pass filter (van Dierendonck et al., 1993):

$$\mathrm{SI} = \frac{\mathrm{SI}_{\mathrm{raw}}}{\mathrm{SI}_{\mathrm{filter}}}. \tag{6}$$

Similar to S_4, the phase scintillation index, σ_φ is defined as the standard deviation of the carrier phase that has been detrended by the 6th-order Butterworth high-pass filter with the cutoff frequency of 0.1 Hz:

$$\sigma_\varphi = \sqrt{\langle \varphi^2 \rangle - \langle \varphi \rangle^2}, \tag{7}$$

where $\langle\ \rangle$ denotes the expected value in 60 s, and φ is the detrended carrier phase.

In addition, the *v*ROTI is also often used to represent the fluctuation of TEC, which is defined as:

$$v\mathrm{ROTI} = \sqrt{\frac{\langle \Delta\mathrm{VTEC}^2 \rangle - \langle \Delta\mathrm{VTEC} \rangle^2}{\langle \Delta t \rangle^2}}. \tag{8}$$

Here we use a slightly different approach where we calculate the *v*ROTI using the vertical TEC (VTEC) (e.g., Juan et al., 2017), where VTEC is given based on equation (1):

$$\mathrm{VTEC} = \frac{1}{M(\epsilon)} \frac{f_i^2 f_j^2}{40.308\left(f_i^2 - f_j^2\right)} \left(L_i - L_j\right), \tag{9}$$

and $M(\epsilon)$ is the obliquity factor, which depends on the satellite elevation ϵ (e.g., Schaer, 1999). It is noted that the calculated VTEC here includes an integer ambiguity, but as we only focus on its relative change, the integer ambiguity does not affect the values of *v*ROTI.

From the definition above, we see that the detrended phase and σ_φ can be derived for each carrier frequency, while the IFLC and *v*ROTI are calculated based on a combination of phases from two carriers. Different from the IFLC from which the refraction part of phase variation has been removed, large TEC gradients, regardless caused by small-scale or large-scale ionospheric structures will cause fluctuations of *v*ROTI. Therefore, the *v*ROTI reflects both the refraction and diffraction-driven phase variations.

We want to note that for this study we considered only measurements from the GPS, as the physics relies on the same for the other GNSS constellations, e.g., GLONASS, Galileo, or Beidou. In addition, we considered only the data with high elevation angles (>40°), to reduce the influence of multipath effects on our results.

3 Results

3.1 The solar wind and geomagnetic conditions during the geomagnetic storm on 7–8 September 2017

During 6–10 September 2017, the Sun released dozens of M-class and four X-class flares, as well as several powerful interstellar coronal mass ejections, causing prominent disturbances in the near-earth space environment and interfering with radio signal propagation (e.g., Blagoveshchensky & Sergeeva, 2019). From top to bottom, Figure 1b shows the variation of the solar wind velocity (VSW), the three components of the interplanetary geomagnetic field (IMF) in geocentric-solar-magnetospheric coordinates, the geomagnetic index *SYM-H,* and the 3-hour *Kp* index. The solar wind velocity increased abruptly around 23:00 universal time (UT) on September 7 and reached a maximum around 07:00 UT on September 8, reaching 800 km/s. Other indices also showed significant changes at the same time, with *Bz* showing an abrupt drop, reaching a minimum of −31 nT around 23:30 UT on September 7. SYM-H also dropped rapidly, reaching a minimum of −146 nT at 01:00 UT on September 8, and the global 3-hour *Kp* index reached above 7 during this period. The indices remained significantly perturbed during the daytime on September 8, and on September 9 the solar wind and geomagnetic indices started to recover.

3.2 Ionospheric scintillation characteristics during the geomagnetic storm

We first analyzed the GPS measurements received at the KHO station and focused on the pseudo-random noise (PRN) codes with dual-frequency signals. Figure 2 shows an overview of the variations of the above-mentioned five indices from September 6–10. Generally enhanced scintillation is observed around noon on September 6, midnight on September 7, and the whole day on September 8. Scintillation around noon of September 6 should be related to the X9.3 solar flare (e.g., Berdermann et al., 2018), while the latter two periods correspond to the initial and main phases of the geomagnetic storm, which also suggests that there are much more small-scale plasma irregularities at high latitude during the geomagnetic storm. One feature seen in Figure 2 is that the five indices didn't always show simultaneous disturbances. When the high-pass filter with a standard cutoff frequency at 0.1 Hz was applied to the carrier phase, the remaining refraction effects are expected to still exist in the detrended phase and σ_φ. As *v*ROTI is sensitive to the TEC gradients of both small-scale and large-scale (Bhattacharyya et al., 2000), it is considered to be affected by both the refraction and diffraction effects. The IFLC is considered to eliminate effectively the refraction

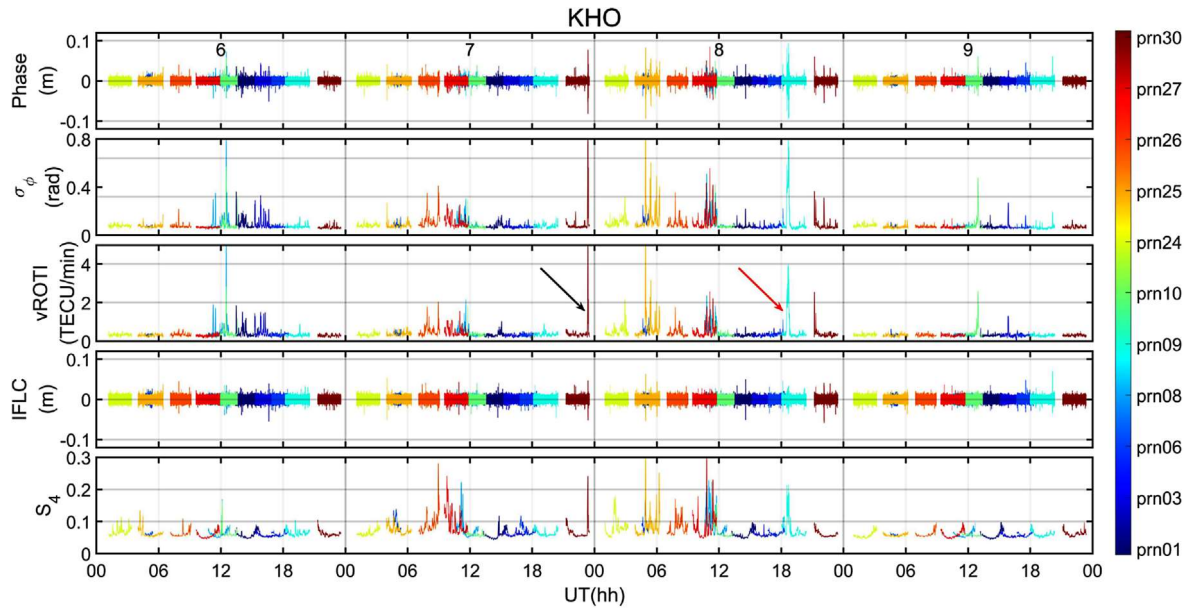

Figure 2. Detrended phase, σ_φ, *v*ROTI, IFLC, and S_4 at the KHO station during 6–9 September 2017. Here, the detrended phase, σ_φ and S_4 are derived from the L5 carrier, while the *v*ROTI and IFLC are calculated by combining the phase measurements on L1 and L5. The black arrow indicates the period of the most intense perturbation of near-earth space, the red arrow indicates the event shown in Figure 3.

effect, and the amplitude scintillation S_4 is mainly influenced by diffraction. Therefore, comparing the simultaneous variations of these different indices provides a possible way to distinguish the refractive and diffractive influences of scintillation.

Figure 3 focuses on the scintillation event observed between 18:00–21:00 UT on September 8, as the signals of PRN = 09 showed the most prominent phase fluctuations (see the interval indicated by a red arrow in Fig. 2). For comparison, variations of these indices during the same UT hours on the other four days are also shown. In Figures 3a and 3b, the variations of the detrended phase, σ_φ, and S_4 are presented separately for L1 and L5, while the *v*ROTI and IFLC are repeated as they combine measurements from both carriers. Compared to the other four days, the detrended phase and σ_φ, as well as the *v*ROTI show clear fluctuations between 18:27 and 18:51 UT on September 8. As expected most of these phase fluctuations are not seen in IFLC, suggesting that the refraction effect dominates the GPS phase and *v*ROTI fluctuations. The remaining fluctuations in IFLC, as well as the fluctuations of amplitude scintillation index, S_4, should be related to the diffraction effects, suggesting the presence of plasma irregularities with sizes less than Fresnel-scale along the wave propagation path.

To have a further look at the refraction and diffraction contributions on the carrier phases, we zoomed in on the detrended phase, *v*ROTI and IFLC for the signals of PRN = 09. Figure 4 shows the results during 18:27–18:51 UT on the geomagnetic quiet (September 6) and disturbed (September 8) days. Compared to September 6, the scintillation effect on the phases reaches about 0.1 m during the considered 20 min on September 8, and the IFLC shows also clear fluctuations with a maximum value reaching 0.05 m at 18:41 UT, showing the effect of non-refractive effects.

In the next step, we calculated the power spectrum of the detrended phase and IFLC of the GPS signal on September 6–9. We considered only data from elevation angles greater than 40°. As a first try, the indices during the whole day are used here to obtain the spectra shown in Figure 5. The power spectra of detrended phases on both L1 and L5 show very similar frequency dependence as that of IFLC on September 6, 7, and 9, suggesting that the applied high-pass filter with a cutoff frequency of 0.1 Hz has effectively removed the refractive variations of the carrier phase. The IFLC has slightly larger values at higher frequencies, which might be due to the fact that the linear combination of IFLC amplifies the high-frequency noise, as the phase is multiplied by a factor larger than the wavelength in the linear combination. Quite differently, the power spectrum of IFLC on September 8 is significantly lower than the power spectra of L1 and L5 at the lower frequencies (<3 Hz). Obviously, this is due to the removal of the refraction effect of IFLC at lower frequencies. It also indicates that the plasma drift velocity is significantly enhanced during the geomagnetic storm, resulting in the Fresnel frequency exceeding 0.1 Hz.

To better quantify the frequency related to non-refraction influences, we limited our analysis to the data when prominent scintillations were observed between 18:27 and 18:51 UT on September 8, as shown in Figure 3. The power spectra of the detrended phase, IFLC, and signal amplitude are shown in Figure 6. Here we only show the results for L5, as the power spectra for L1 are very similar. Compared to the detrended phase for different days, the power spectrum in the entire frequency range is greater when the prominent scintillation is observed on September 8. For IFLC on September 8 the power spectrum is slightly higher at frequencies above 1 Hz compared to the other days, which indicates that the non-refractive effect mainly exists for frequencies larger than 1 Hz. This is confirmed by the power spectrum of the signal

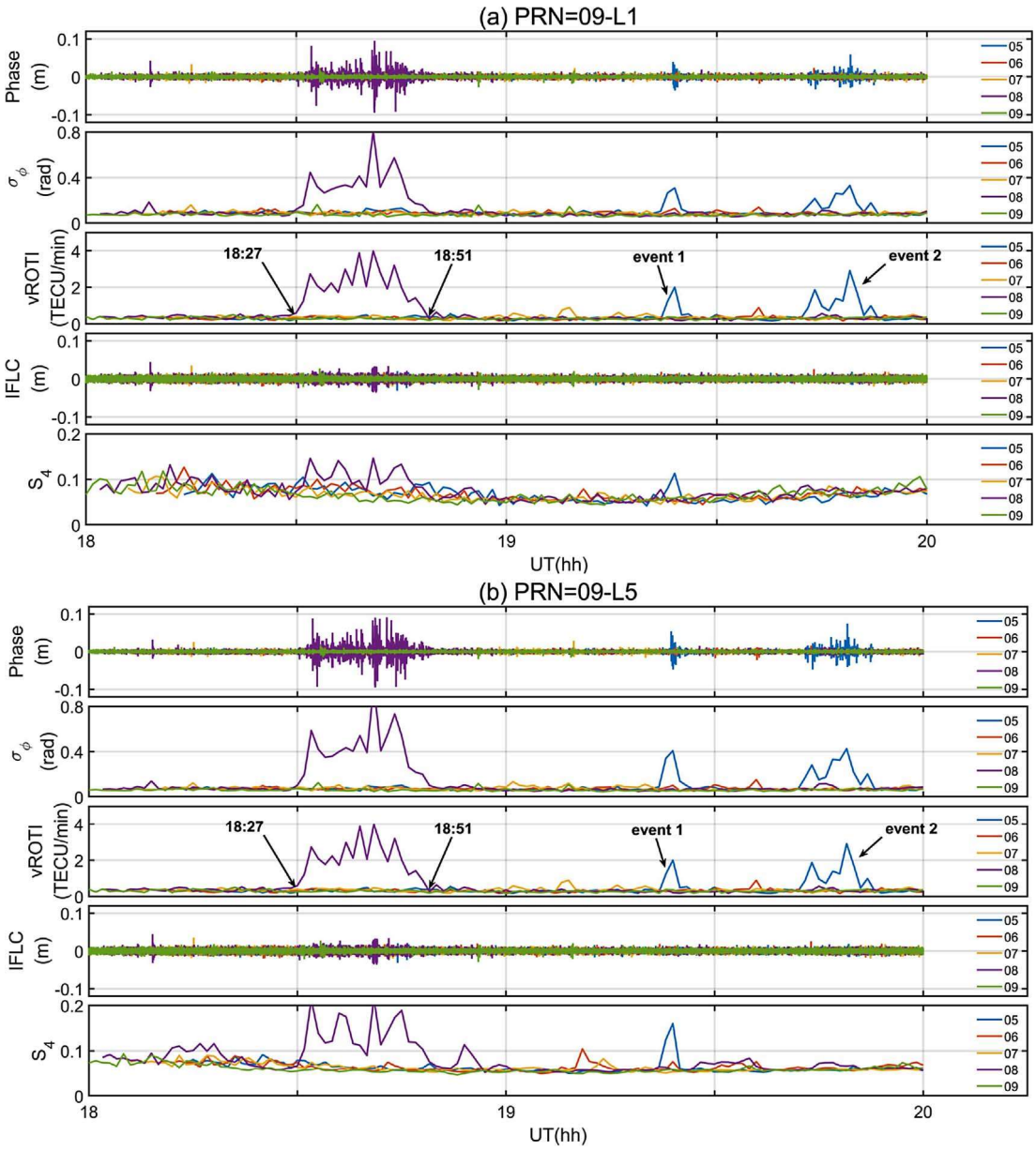

Figure 3. Detrended phase, σ_φ, *v*ROTI, IFLC, and S_4 of PRN = 09 at the KHO station during 18:00–21:00 UT on 5–9 September 2017. Results for the carrier L1 and L5 are presented separately in Figures 3a and 3b. Different colors represent different dates. Black arrows point to several distinct scintillation events.

amplitude shown in the bottom panel, as diffraction mainly affects the signal amplitude, which shows higher values for frequencies less than 5 Hz. By fitting the different frequency ranges of the power spectrum of the signal amplitude, two typical features are identified: a nearly flat value for frequencies below 1 Hz, and a power-law spectrum for frequencies between 1 and 5 Hz. As explained by Yeh & Liu (1982), the later part following the power-law spectrum is related to the diffraction caused by the plasma irregularities smaller than the Fresnel scale size. As no significant amplitude fluctuations are seen following the power-law spectrum on September 6, 7, and 9, it indicates an absence of plasma irregularities less than the Fresnel scale size.

Figure 7 highlights the ratio between the detrended phases on L5 and L1 from 18:28 to 18:51 UT. According to the different power spectral features shown in Figure 6, the data have been divided into frequency bins of 0.1–1 Hz, 1–5 Hz, and 5–25 Hz, representing pure refraction, diffraction-modulated refraction, and high-frequency noise, respectively. To visualize the relationship between the dual-frequency phase, linear regression is used to fit the series of detrended phases in the three different frequency ranges. On September 6 (top of Fig. 7) there was no significant scintillation observed. The fitted slopes in the three frequency intervals are 1.00, 0.77, and 0.53, and the correlations are 0.97, 0.74, and 0.46, respectively. The phases of L1 and L5 show good uniformity in the low-frequency

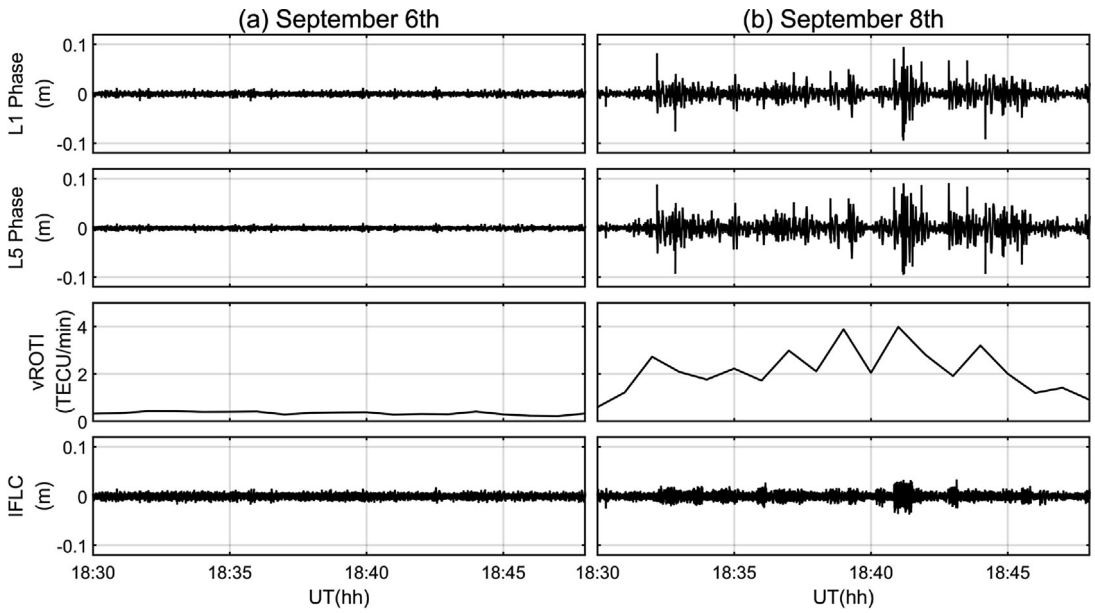

Figure 4. Zoomed in for the detrended phase on L1 and L5, *v*ROTI, and IFLC of PRN = 09 at the KHO station on (a) 6 September 2017, and (b) 8 September 2017.

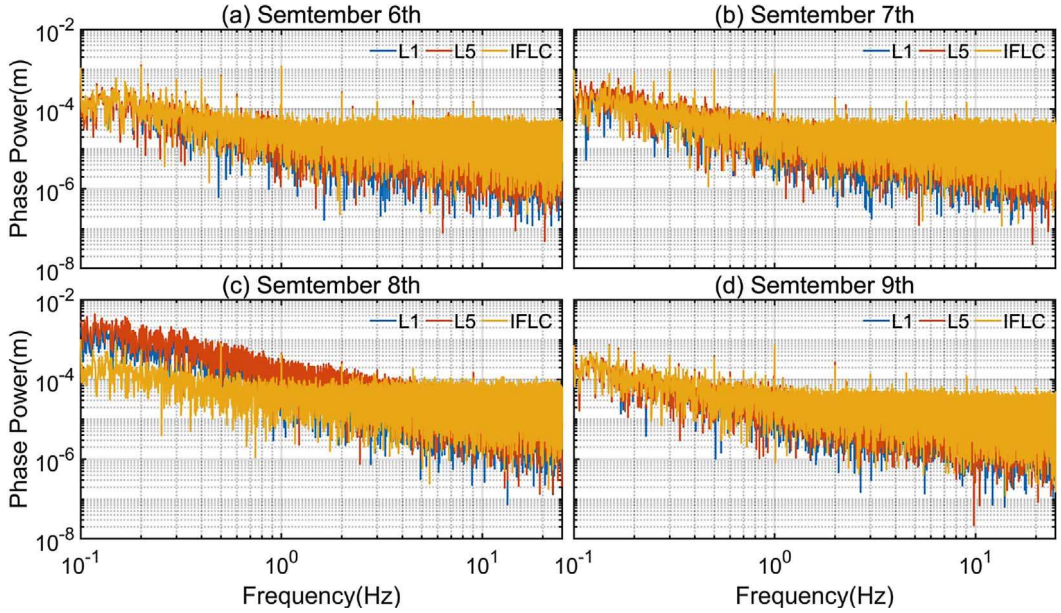

Figure 5. Power spectra of detrended phase of L1 (blue) and L5 (red), as well as IFLC (yellow) from 6–9 September 2017.

interval, indicating that the refraction effect during the geomagnetic quiet period is well removed by the Butterworth filtering at 0.1 Hz. In the middle and high-frequency ranges, the fitting slopes decrease due to additional random noise. On September 8 (bottom of Fig. 7), when intense scintillation was observed in the same UT interval, a strong linear relation is seen between the detrended phases of L1 and L5, with a fitted slope of 1.72 and a confidence interval [1.717, 1.723], which is very close to the theoretical value of $\frac{f_j^2}{f_i^2} = 1.79$ as indicated in the equation (2). The correlation coefficient also reached as high as 0.99. This result confirms that refraction variations of the detrended carrier phases of L1 and L5 remain in the scintillation event. For the second frequency range, the slope of the linear regression and the correlation coefficient reduces to 1.36 and 0.85, respectively. This result suggests that although refraction dominates the phase variation, additional diffraction appears, leading to a reduced linear relation between the phase variations of L1 and L5. For the third frequency range, the slope of the linear regression decreased to 0.53 and the correlation coefficient was only 0.37, indicating that high-frequency noise dominates.

Moreover, the high-frequency noise seems also to be enhanced on the geomagnetic disturbed day.

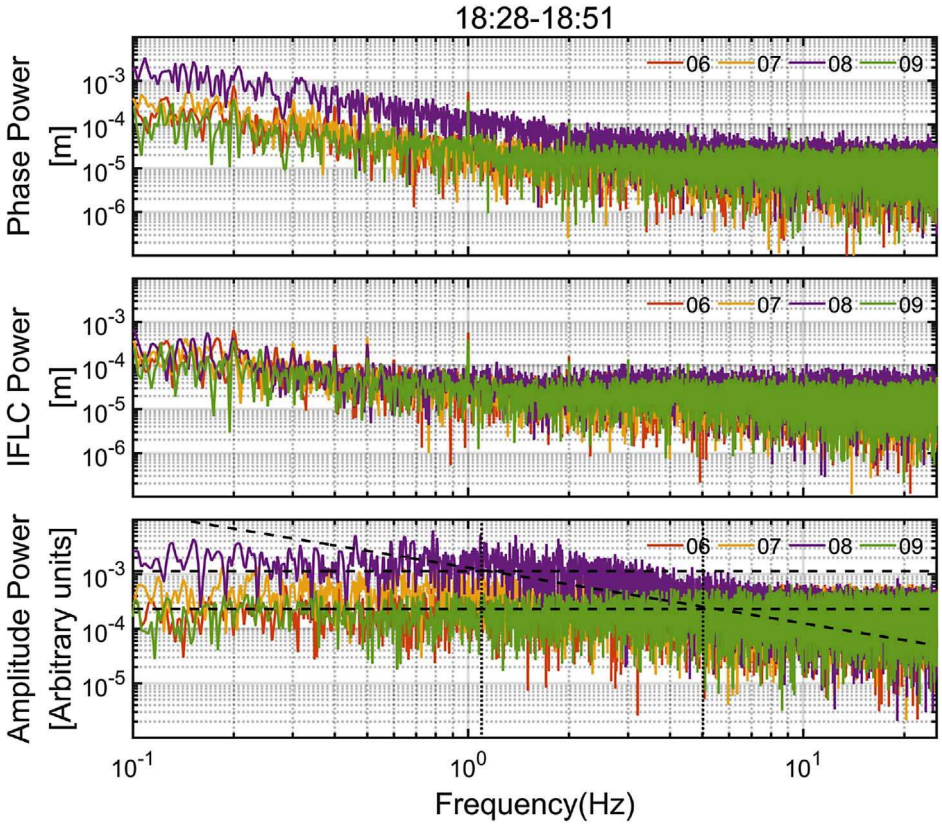

Figure 6. The power spectra of detrended L5 phase, IFLC, and L5 amplitude on different days (marked with different colors) in September 2017. The data considered here are from 18:28–18:51 UT each day, as the most severe scintillation occurred in this UT interval on 8 September 2017.

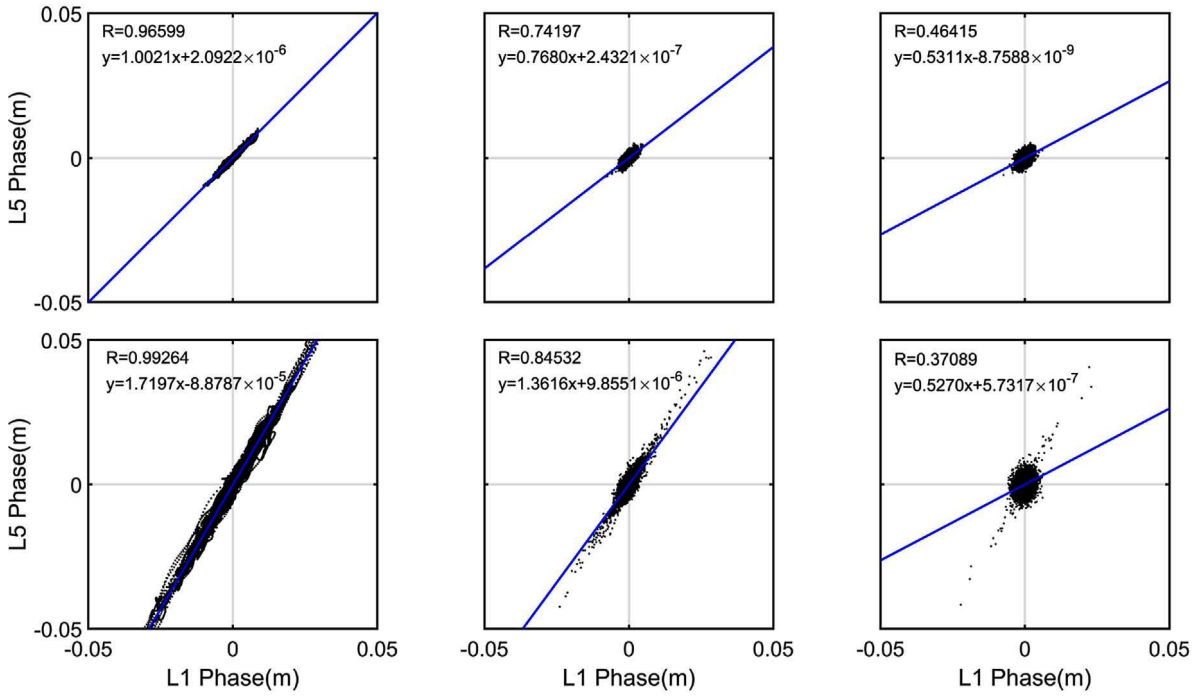

Figure 7. Linear fits for different frequency intervals of phase between L1 and L5 (0.1–1 Hz, 1–5 Hz, 5–25 Hz, respectively), the blue curve shows the results of the fit. The top row is for 6 September 2017, and the bottom row is for 8 September 2017.

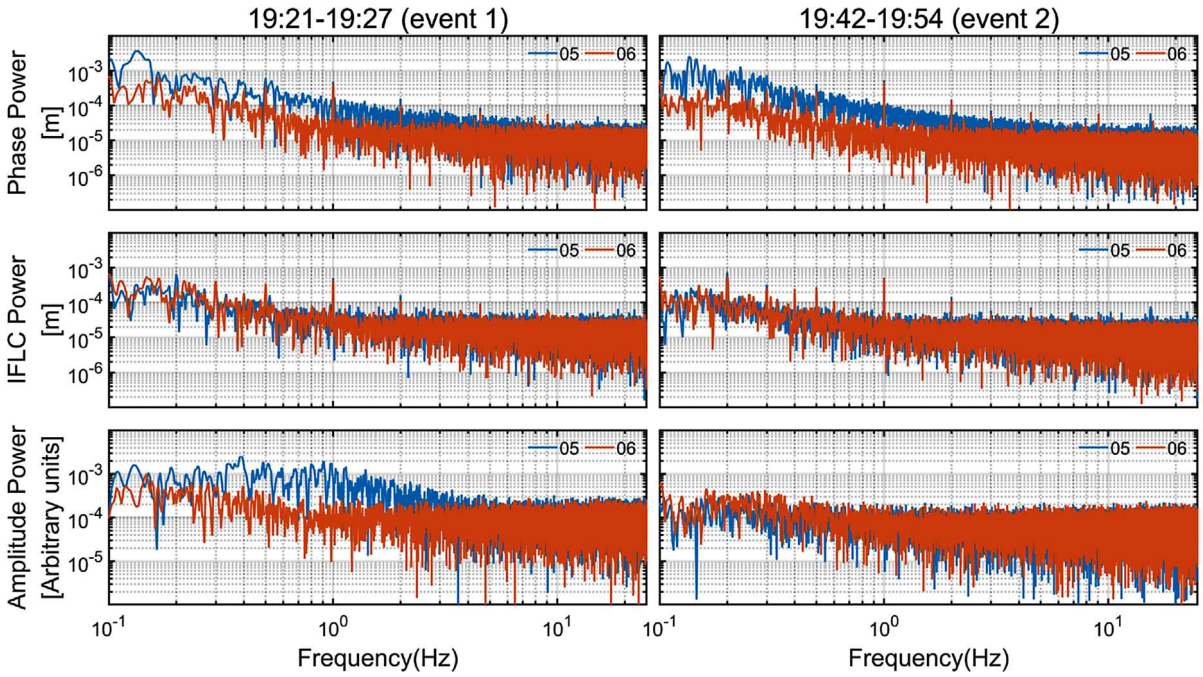

Figure 8. The power spectra of detrended L5 phase, IFLC, and L5 amplitude on 5 September 2017 (blue) and 6 September 2017 (red). The left column shows the results for event 1 observed between 19:21 to 19:27 UT, and the right column shows the results for event 2 observed between 19:42 to 19:54 UT. The data during the same UT intervals on 6 September 2017 are added here as a reference to the situation without scintillation.

All the results presented above originate from the KHO station. However, the other three stations show very similar results during the geomagnetic storm, so we do not repeat those figures here.

3.3 Ionospheric scintillation characteristics before and during the geomagnetic storm

In the previous section, we mainly focused on the occurrence of scintillation during a geomagnetic storm. As we aim to find out different characteristics between scintillation events before and during the geomagnetic storms, in this part we will have a further look at the scintillations observed before the storm (on September 5), marked as event 1 and event 2 in Figure 3. A common feature between the two events is strong fluctuations in the detrended phase, σ_{φ} and νROTI, but with almost no perturbation of IFLC, which is different from the storm-time ionospheric scintillation events discussed in Section 3.2.

We first have a look at the scintillation event 1 occurring from 19:21 to 19:27 UT on September 5. As the variations of power spectra are very similar for L1 and L5, here we only show the results from L5. We see that the power spectrum of the detrended phase at frequencies up to 5 Hz is slightly larger than the values on September 6, which is considered a reference level for the situation without scintillation. The power spectrum of IFLC maintains more or less the same value in the whole frequency range for both days, indicating that the relatively higher power spectrum at times of high scintillation is removed from the IFLC. A further spectrum analysis is shown in Figure 8 to highlight that the phase fluctuations appear mainly in the low-frequency interval, and the IFLC power spectrum is not significantly different compared to the other days, but the amplitude spectral power shows significant fluctuations. That is, the variations of IFLC do not correspond well with that of S_4.

For the scintillation event 2 observed from 19:42 to 19:54 UT on September 5, the detrended L5 phase shows similar features in the power spectrum; frequencies up to 5 Hz are slightly enhanced on September 5 compared to September 6, which has been eliminated in the IFLC. Different from the first event, the power spectrum of the signal amplitude does not show a power-law feature for frequencies 1–5 Hz, which is in fact consistent with the absent S_4 fluctuations of event 2 as shown in Figure 3b. It also suggests that the event 2 is dominated by the refraction effect, without a significant contribution from diffraction and other high-frequency noise.

To better understand the power spectrum of scintillations before and during the geomagnetic storm, we further show the relative power spectra for the four scintillation events discussed above. The relative spectra are derived by subtracting their averaged spectra on the other four days when no scintillation is observed. In addition, a 2 Hz wide moving boxcar is applied to smooth out the fast variations in the relative power spectra. The result is shown in Figure 9. A prominent feature in the top panel is that the IFLC has a generally higher power spectrum at all frequencies for the scintillation events on September 7 and 8 (during the geomagnetic storm), while the other two scintillation events observed on September 5 (before the geomagnetic storm) have a lower spectrum. Looking at the two events on September 5, the relative power spectrum of IFLC is also slightly higher for event 1 (with amplitude scintillation) than for event 2 (without amplitude scintillation). For the

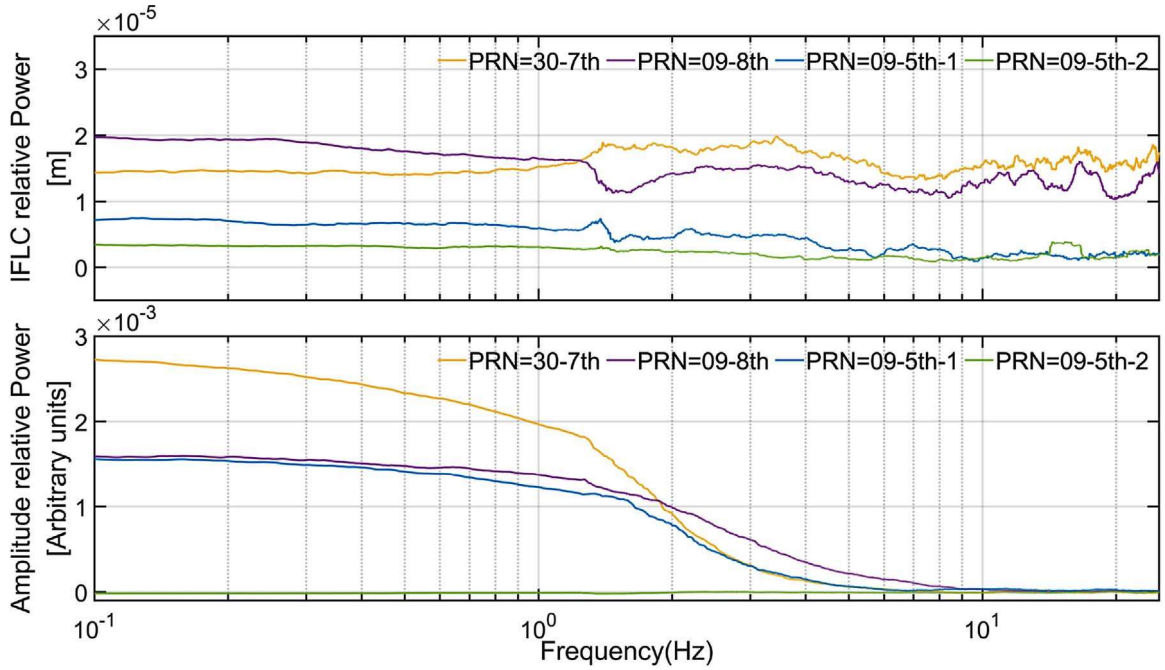

Figure 9. Relative power spectra of IFLC and signal amplitude for four scintillation events during and before the geomagnetic storm. PRN = 30–7th represents the scintillation event that occurred at midnight on 7 September 2017, as marked by the black arrow in Figure 2, corresponding to the period of the most intense perturbation of near-earth space in Figure 1b. PRN = 09–8th represents the scintillation event that occurred on 8 September 2017, as marked by the red arrow in Figure 2. PRN = 09–5th-1 and PRN = 09–5th-2 represent the scintillation events on 5 September 2017 from 19:21 to 19:27 UT and 19:42 to 19:54 UT, respectively.

spectra of signal amplitude (bottom panel), event 1 on September 5 shows a very similar spectrum variation to the two events during the geomagnetic storm. In addition, a clear power-law spectrum is seen at frequencies roughly from 1.5 to 5 Hz, suggesting that the diffraction effect dominates in this frequency range for all three scintillation events. For event 2 on September 5, the power spectrum of the signal amplitude stays at a very low value in the whole frequency range, indicating the absence of the diffraction effect.

4 Discussions

4.1 Scintillation classification by different indices

Though different indices were proposed to reflect or monitor ionospheric scintillation, they do not always show simultaneous fluctuations when scintillation occurs. The detrended carrier phase and σ_{φ} are directly related to the phase variations. As mentioned in the Introduction, applying a high-pass filter to the carrier phase is a common approach to remove the refraction-driven variations. However, the plasma drift velocity at high latitudes can vary by one or two orders of magnitude, so setting the cutoff frequency of the high-pass filter (corresponding to the Fresnel frequency) at a fixed threshold (e.g., 0.1 Hz) is not a promising way for the carrier phase processing a high latitude (e.g., Wang et al., 2018; McCaffrey & Jayachandran, 2019). Consequently, both refraction and diffraction effects can co-exist in the indices, detrended phase and σ_{φ}.

The index *v*ROTI has combined the phase measurements from two carriers and is defined as the rate of change of TEC, so it is sensitive to the gradient of TEC. As seen from in-situ electron density measurements from low Earth orbiting (LEO) satellites, the post-sunset equatorial plasma bubble (e.g., Su et al., 2006; Stolle et al., 2008; Xiong et al., 2010) and high-latitude plasma patches (e.g., Jin et al., 2014; Xiong et al., 2019) are usually associated with strong plasma density gradient at the meso-scale size. Therefore, the *v*ROTI is useful for tracing these meso-scale irregular structures. However, as pointed out by Bhattacharyya et al. (2000), ROTI can also be elevated in the presence of TEC gradients associated with large-scale ionospheric structures, e.g., at the crest edge of the equatorial ionization anomaly (EIA). This feature is especially prominent for the ROTI derived from the receiver onboard high-inclination LEO satellites, which usually have a speed of 7.5 km/s to fly through the equatorial and poleward edges of the EIA crest within a few minutes. From this perspective, the fluctuations in *v*ROTI are caused by not only the diffraction (gradient associated with small-scale structures) but also the refraction (gradient associated with large-scale structures) effects (e.g., Spogli et al., 2013; Demyanov et al., 2019). This also explains why the ROTI at high latitudes often shows consistent fluctuations with the detrended carrier phase and σ_{φ}, though they are not always consistent (Jin et al., 2017). In addition, the sampling interval (Carrano & Groves, 2007; Demyanov et al., 2019; Li et al., 2022) and viewing geometry between the receiver and GNSS satellite ray path (Yang & Liu, 2016) both have a significant influence on the ROTI derivation. Therefore, additional care must be taken for interpreting the variations of ROTI (Carrano et al., 2019).

Similar to *v*ROTI, IFLC is also calculated by combining phase measurements of two carriers. However, the refraction

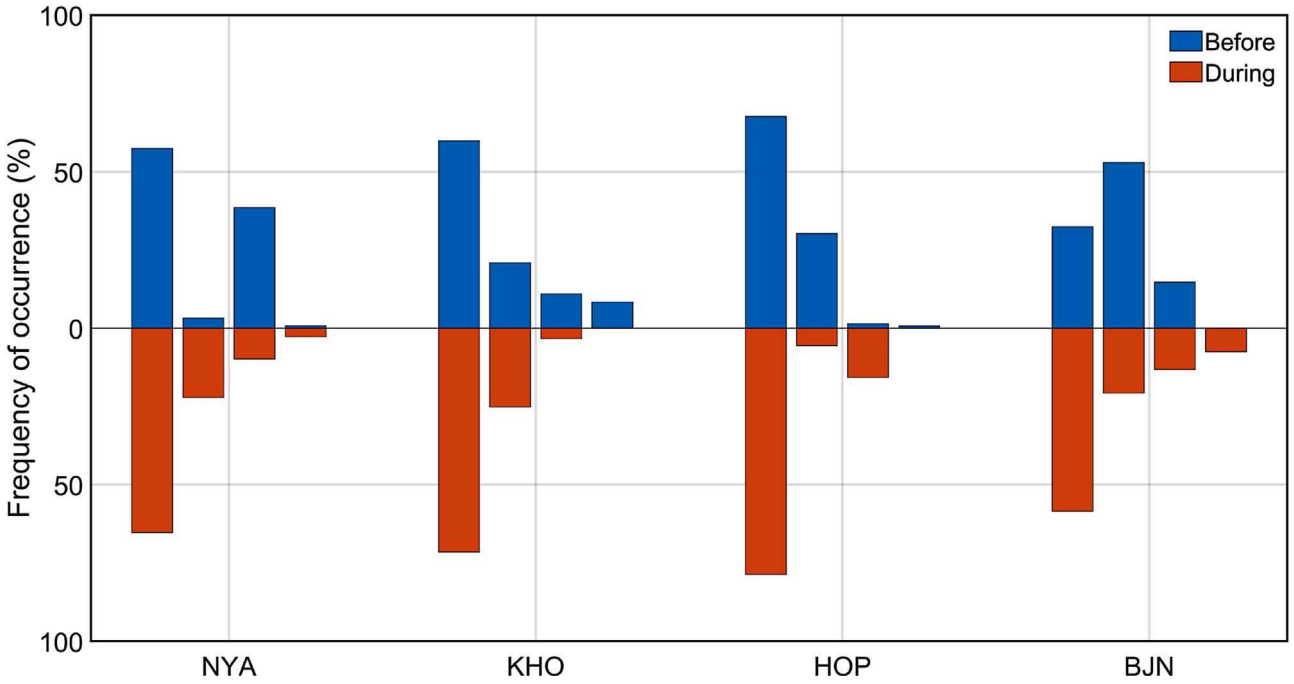

Figure 10. Occurrence ratios of the four types of scintillation events observed from the four Svalbard stations in Norway. For each station, the events from left to right represent: (1) phase indices, IFLC, and S_4 all show fluctuations; (2) both phase indices and S_4 show fluctuations, but not IFLC; (3) both phase indices and IFLC show fluctuations, but not S_4; (4) only phase indices show fluctuation, but not IFLC and S_4. Events before (5–6 September 2017) and during (7–8 September 2017) the geomagnetic storm are represented by blue and red colors, respectively.

contribution has been removed as seen in equation (4). Therefore, the remaining fluctuations in IFLC are mainly related to diffraction and high-frequency noise. As the amplitude scintillation index, S_4 is also only attributed to the diffraction effect, it is expected that the S_4 will show consistent variations with IFLC if the high-frequency noise has been ignored. This is true for the scintillation from 18:27 to 18:51 UT on September 8 and scintillation event 2 on September 5 (see Fig. 3). The IFLC and S_4 show consistent variations, with prominent fluctuation and no fluctuation in the two events, which also suggests that the diffraction effect exists and is absent in the two events, respectively. Quite different is the scintillation event 1 on September 5, as only S_4 show a clear enhanced value (persisting for about 6 min), and no clear fluctuation is seen in the IFLC. A possible reason for the difference between IFLC and S_4 will be discussed in Section 4.2.

As discussed above, we have further roughly divided the scintillation events into four categories: (1) phase indices, IFLC, and S_4 all show simultaneous fluctuations; (2) both phase indices and S_4 show simultaneous fluctuations, but not IFLC; (3) both phase indices and IFLC show simultaneous fluctuations, but not S_4; (4) only phase indices show fluctuation, but not IFLC and S_4. The fluctuation is defined if the index variation is greater than three times its standard deviation over the entire observed time period.

The occurrence ratio of the four types of scintillation events from the four Svalbard stations in Norway is shown in Figure 10. The results before (September 5 and 6) and during (September 7 and 8) the geomagnetic storm are presented in blue and red colors, respectively. We see the first and second types of events belong to the majority, and the first type is the most common, while the third and fourth types are relatively rare. In addition, the first type is more frequent during the geomagnetic storm than before the storm, and it is true for all four stations, while the other three types do not show any consistent storm dependence among the four stations.

4.2 Relation between IFLC and S_4

As seen from equation (4), the IFLC is good to reflect the diffraction effect, therefore it is expected to correspond well with the variations of S_4. However, as indicated by the second and third types of events in Figure 10, the IFLC does not always correspond well to S_4. To better investigate the relationship between the two indices, we performed a statistical analysis of scintillation events before and during the geomagnetic storms, and the result is shown in Figure 11. No clear linear regression is seen between the S_4 and IFLC. The absolute values of IFLC before the geomagnetic storm are generally lower than that during the geomagnetic storms, but such a feature is not seen in S_4. Such a storm dependence on IFLC explains the increased occurrence of the first type of events during the geomagnetic storm.

As mentioned earlier, diffraction-modulated refraction effects can be divided into pure refraction effects and diffraction effects. The former frequency is mainly affected by the rate of electron density change associated with irregularity (e.g., Kintner et al., 2007), while the latter depends on the irregularity drift velocity relative to the ionospheric piercing point (McCaffrey et al., 2018). Therefore, the signal received by the receiver is a superposition of both the refraction and diffraction-modulated

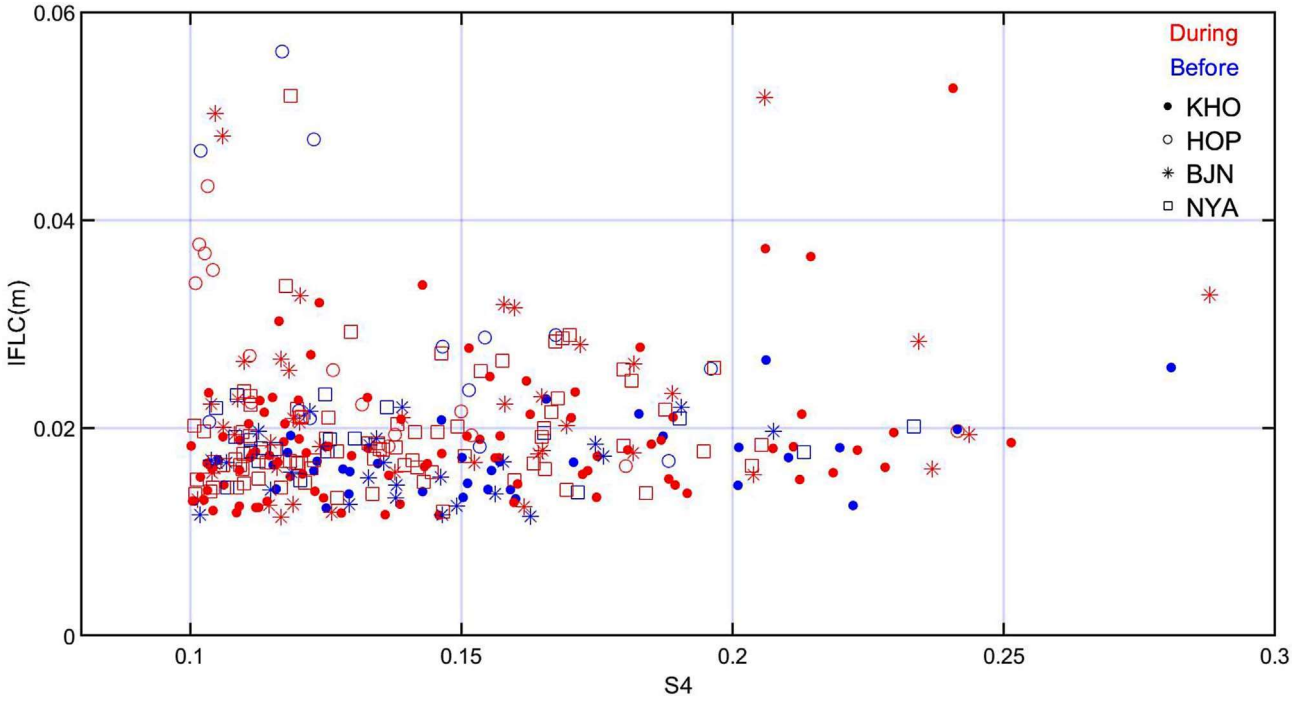

Figure 11. The IFLC and S_4 variations for scintillation events observed from 5–8 September 2017. Scintillation events before (5–6 September 2017) and during (7–8 September 2017) the geomagnetic storm are presented in blue and red colors. Scintillation events from the four different stations are marked with different symbols.

signals. Let's take a simple sine wave signal with a fixed frequency as an example, the superimposed signal satisfies the:

$$\begin{cases} S_r = A_r \cos(\omega t - \boldsymbol{k}\cdot\boldsymbol{r} + \varphi_r) \\ S_d = A_d \cos(\omega t - \boldsymbol{k}\cdot\boldsymbol{r} + \varphi_d) \\ S = S_r + S_d = A\cos(\omega t - \boldsymbol{k}\cdot\boldsymbol{r} + \varphi) \\ A = \sqrt{A_d^2 + A_r^2 + 2A_rA_d\cos(\varphi_r - \varphi_d)} \\ \varphi = \arctan\left(\dfrac{A_r\sin(\varphi_r) + A_d\sin(\varphi_d)}{A_r\cos(\varphi_r) + A_d\cos(\varphi_d)}\right) \end{cases}, \quad (10)$$

where S_r is the refraction signal, S_d is the diffraction signal, A_r is the amplitude of the refraction signal, A_d is the amplitude of the diffraction signal, φ_r is the phase change of the signal due to refraction, φ_d is the phase change of the signal due to diffraction, ω is the angular velocity, t is the signal propagation time, $\boldsymbol{k}$ is the wave vector, $\boldsymbol{r}$ is the signal propagation distance.

When A_r equals to A_d, the last two relations simplify to:

$$\begin{cases} A = 2A_r\cos\left(\dfrac{\varphi_r - \varphi_d}{2}\right) \\ \varphi = \dfrac{\varphi_r + \varphi_d}{2} \end{cases}. \quad (11)$$

From equation (11), we see that the amplitude of the superimposed signal is jointly affected by diffraction and refraction effects, and their relative contributions to the final amplitude variation are uncertain for different scintillation events. However, the refraction and diffraction contributions to the phase of the superimposed signal are linearly additive. Although the IFLC has removed the refraction part, the diffraction-driven phase variation in IFLC is still additive. This is only a simplified consideration, a more rigorous theory can be found in the related studies of the model (e.g., Gherm et al., 2005). In real ionospheric scintillation, the diffraction and refraction contributions are not equal, which will lead to a non-linearly additive part of the phase. And their joint effect should be obtained by the integration rather than a simple summation. In addition, the diffraction effect on the two carrier signals (L1 and L5) does not correlate well, and since IFLC is a combination of two carrier signals, the diffraction effect embodied by IFLC is even less likely to correlate well with the diffraction effect on the amplitude. It is also important to note that the low magnitude diffractive variations are eliminated in IFLC as well (McCaffrey & Jayachandran, 2019), which may lead to the easier observation of S_4 fluctuations compared to IFLC, as shown in event 1 in Figure 8. But there is no doubt that the increase in high-frequency power is clearly seen in the phase power spectrum during the geomagnetic storm (as shown in Fig. 9), which leads to an increase of IFLC during the geomagnetic storm. In contrast, in the amplitude power spectrum, we can only see the effect of diffraction, and no increase in high-frequency power is found in the amplitude power spectrum before and during the geomagnetic storm. We suggest that the enhanced IFLC during the geomagnetic storm is caused by the increased high-frequency phase power, which should be related to the enhanced density of small-scale irregularities during storm periods. Moreover, in the IFLC frequency relative spectrum

of Figure 9, we can see that the increase of IFLC during the geomagnetic storm is in the full frequency interval. We cannot exclude that the increase of IFLC during the geomagnetic storm is also influenced by diffraction and refraction (higher-order influence of the refraction effect and the change of the refraction path) enhancement. The enhancement of diffraction may be due to the increase in the number of Fresnel-scale plasma irregularities in the ray path.

5 Summary

In this study, we used the high-resolution (50 Hz) phase and amplitude measurements from four high-latitude GNSS stations in Svalbard (Norway), for investigating the refractive and diffractive contributions to the ionospheric scintillation during the geomagnetic storm on 7–8 September 2017. The main findings are:

1. At high latitudes, the high-pass filter with a standard cut-off frequency at 0.1 Hz sometimes cannot effectively remove the refraction-driven phase variation, especially during a geomagnetic storm, leading to remaining refraction contribution to the detrended carrier phase and σ_{φ} when scintillation occurs, while IFLC can better represent phase variations driven by non-refraction effects. In the meanwhile, as *v*ROTI is sensitive to the TEC gradients, regardless of small- or large-scale ionospheric structures, therefore both refraction and diffraction effects can cause fluctuation of *v*ROTI.
2. For most of the scintillation events during the geomagnetic storm, the phase indices (including detrended carrier phase, σ_{φ}, and *v*ROTI), IFLC and S_4 show consistent fluctuations, indicating the diffraction effect usually occur simultaneously with the refraction effect during active scintillation.
3. Both the IFLC and S_4 were thought to be related to the diffraction effect. Although they respond simultaneously, they are not always correlated, which is the result of multiple factors. The IFLC seems to be enhanced during the geomagnetic storm, but such a feature is not seen in S_4. We suggest that the enhanced IFLC during the geomagnetic storm is caused by the increased high-frequency phase power, which should be related to the enhanced density of small-scale irregularities during storm periods.

Acknowledgements. This study is supported by the Special Found of Hubei Luojia Laboratory (220100011) and the National Natural Science Foundation of China (42174191). Chao Xiong is partly supported by the Dragon 5 cooperation 2020–2024 (project no. 59236) and the ISSI-BJ project "The electromagnetic data validation and scientific application research based on CSES satellite". The 50 Hz GPS measurements from the four stations in Svalbard (Norway) were obtained from The University of Bergen Global Navigation Satellite System Data Collection, which is publicly accessible via https://doi.org/10.18710/AJ4S-X394 and supported by the Research Council of Norway (RCN) grant 223252. The editor thanks Anthony McCaffrey and an anonymous reviewer for their assistance in evaluating this paper.

References

Aarons J, Basu S. 1994. Ionospheric amplitude and phase fluctuations at the GPS frequencies. In: Proceedings of the 7th International Technical Meeting of the Satellite Division of The Institute of Navigation (ION GPS 1994), Salt Lake City, UT, September 20–23, pp. 1569–1578.

Aarons J. 1982. Global morphology of ionospheric scintillations. *Proc IEEE* **70(4)**: 360–378. https://doi.org/10.1109/PROC.1982.12314.

Basu S, Mullen JP, Bushby A. 1980. Long-term 1.5 GHz amplitude scintillation measurements at the geomagnetic equator. *Geophys Res Lett* **7(4)**: 259–262. https://doi.org/10.1029/GL007i004p00259.

Beach TL. 2006. Perils of the GPS phase scintillation index (σ_{ϕ}). *Radio Sci* **41(5)**: 1–7. https://doi.org/10.1029/2005RS003356.

Berdermann J, Kriegel M, Banyś D, Heymann F, Hoque MM, Wilken V, Borries C, Heßelbarth A, Jakowski N. 2018. Ionospheric response to the X9.3 flare on 6 September 2017 and its implication for navigation services over Europe. *Space Weather* **16(4)**: 1604–1615. https://doi.org/10.1029/2018SW001933.

Bhattacharyya A, Beach TL, Basu S, Kintner PM. 2000. Nighttime equatorial ionosphere: GPS scintillations and differential carrier phase fluctuations. *Radio Sci* **35(1)**: 209–224. https://doi.org/10.1029/1999RS002213.

Bittencourt JA. 2004. *Fundamentals of plasma physics*, 3rd edn. Springer, New York. ISBN 978-1-4419-1930-4.

Blagoveshchensky DV, Sergeeva MA. 2019. Impact of geomagnetic storm of September 7–8, 2017 on ionosphere and HF propagation: A multi-instrument study. *Adv Space Res* **63(1)**: 239–256. https://doi.org/10.1016/j.asr.2018.07.016.

Booker HG, Ratcliffe JA, Shinn DH. 1950. Diffraction from an irregular screen with applications to ionospheric problems. *Philos Trans R Soc A* **242(856)**: 579–609. https://doi.org/10.1098/rsta.1950.0011.

Carrano CS, Groves KM, McNeil WJ, Doherty PH. 2013. Direct measurement of the residual in the ionosphere-free linear combination during scintillation. In: Proceedings of the 2013 Institute of Navigation ION NTM Meeting, San Diego, CA, January 28–30, pp. 585–596.

Carrano CS, Groves KM, Rino CL. 2019. On the relationship between the rate of change of total electron content index (ROTI), irregularity strength (C_kL), and the scintillation index (S_4). *J Geophys Res: Space Phys* **124(3)**: 2099–2112. https://doi.org/10.1029/2018JA026353.

Carrano CS, Groves KM. 2007. TEC gradients and fluctuations at low, latitudes measured with high data rate GPS receivers. In: Proceedings of the 63rd Annual Meeting of The Institute of Navigation, Cambridge, MA, April 23–25, 2007, 156–163.

Carrano CS, Rino CL. 2016. A theory of scintillation for two-component power law irregularity spectra: overview and numerical results. *Radio Sci* **51(6)**: 789–813. https://doi.org/10.1002/2015RS005903.

Cordes JM, Pidwerbetsky A, Lovelace RVE. 1986. Refractive and diffractive scattering in the interstellar medium. *Astrophys J* **310**: 737–767. https://doi.org/10.1086/164728.

Demyanov VV, Yasyukevich YV, Jin S, Sergeeva MA. 2019. The second-order derivative of GPS carrier phase as a promising means for ionospheric scintillation research. *Pure Appl Geophys* **176**: 4555–4573. https://doi.org/10.1007/s00024-019-02281-6.

Emmert JT, Richmond AD, Drob DP. 2010. A computationally compact representation of Magnetic-Apex and Quasi-Dipole coordinates with smooth base vectors. *J Geophys Res: Space Phys* **115(A8)**: A08322. https://doi.org/10.1029/2010JA015326.

Forte B, Radicella SM. 2002. Problems in data treatment for ionospheric scintillation measurements. *Radio Sci* **37(6)**: 1–8. https://doi.org/10.1029/2001RS002508.

Forte B. 2005. Optimum detrending of raw GPS data for scintillation measurements at auroral latitudes. *J Atmos Terr Phys* **67(12)**: 1100–1109. https://doi.org/10.1016/j.jastp.2005.01.011.

Gherm VE, Zernov NN, Strangeways HJ. 2005. Propagation model for transionospheric fluctuating paths of propagation: Simulator of the transionospheric channel. *Radio Sci* **40(1)**: RS1003. https://doi.org/10.1029/2004RS003097.

Ghobadi H, Spogli L, Alfonsi L, Cesaroni C, Cicone A, Linty N, Romano V, Cafaro M. 2020. Disentangling ionospheric refraction and diffraction effects in GNSS raw phase through fast iterative filtering technique. *GPS Solut* **24**: 85. https://doi.org/10.1007/s10291-020-01001-1.

Jin Y, Moen JI, Miloch WJ. 2014. GPS scintillation effects associated with polar cap patches and substorm auroral activity: direct comparison. *J Space Weather Space Clim* **4**: A23. https://doi.org/10.1051/swsc/2014019.

Jin Y, Moen JI, Oksavik K, Spicher A, Clausen LBN, Miloch WJ. 2017. GPS scintillations associated with cusp dynamics and polar cap patches. *J Space Weather Space Clim* **7**: A23. https://doi.org/10.1051/swsc/2017022.

Juan JM, Aragon-Angel A, Sanz J, Rovira-Garcia A. 2017. A method for scintillation characterization using geodetic receivers operating at 1 Hz. *J Geod* **91**: 1383–1397. https://doi.org/10.1007/s00190-017-1031-0.

Kashcheyev A, Nava B, Radicella SM. 2012. Estimation of higher-order ionospheric errors in GNSS positioning using a realistic 3-D electron density model. *Radio Sci* **47(4)**: RS4008. https://doi:10.1029/2011RS004976.

Kintner PM, Ledvina BM, de Paula ER. 2007. GPS and ionospheric scintillations. *Space Weather* **5(9)**: S09003. https://doi.org/10.1029/2006SW000260.

Li W, Song S, Jin X. 2022. Ionospheric scintillation monitoring with ROTI from geodetic receiver: Limitations and performance evaluation. *Radio Sci* **57(5)**: e2021RS007420. https://doi.org/10.1029/2021RS007420.

McCaffrey AM, Jayachandran PT. 2019. Determination of the Refractive Contribution to GPS Phase "Scintillation". *J Geophys Res: Space Phys* **124(2)**: 1456–1469. https://doi.org/10.1029/2018JA025759.

McCaffrey AM, Jayachandran PT, Langley RB, Sleewaegen JM. 2018. On the accuracy of the GPS L2 observable for ionospheric monitoring. *GPS Solut* **22**: 23. https://doi.org/10.1007/s10291-017-0688-4.

Mushini SC, Jayachandran PT, Langley RB, MacDougall JW, Pokhotelov D. 2012. Improved amplitude- and phase-scintillation indices derived from wavelet detrended high-latitude GPS data. *GPS Solut* **16(4)**: 363–373. https://doi.org/10.1007/s10291-011-0238-4.

Oksavik K. 2020. *The University of Bergen Global Navigation Satellite System Data Collection*. DataverseNO. https://doi.org/10.18710/AJ4S-X394.

Oksavik K, van der Meeren C, Lorentzen DA, Baddeley LJ, Moen J. 2015. Scintillation and loss of lock from poleward moving auroral forms in the cusp ionosphere. *J Geophys Res Space Phys* **120(10)**: 9161–9175. https://doi.org/10.1002/2015JA021528.

Pi X, Mannucci AJ, Lindqwister UJ, Ho CM. 1997. Monitoring of global ionospheric irregularities using the Worldwide GPS Network. *Geophys Res Lett* **24(18)**: 2283–2286. https://doi.org/10.1029/97GL02273.

Rino CL, Fremouw EJ. 1977. The angle dependence of singly scattered wavefields. *J Atmos Terr Phys* **39(8)**: 859–868. https://doi.org/10.1016/0021-9169(77)90166-0.

Rino CL. 1979a. A power law phase screen model for ionospheric scintillation: 1. *Weak scatter. Radio Sci* **14(6)**: 1135–1145. https://doi.org/10.1029/rs014i006p01135.

Rino CL. 1979b. A power law phase screen model for ionospheric scintillation: 2: Strong scatter. *Radio Sci* **14(6)**: 1147–1155. https://doi.org/10.1029/RS014i006p01147.

Schaer S. 1999. Mapping and predicting the earth's ionosphere using the global positioning system, *Ph.D. Thesis*. University of Bern, Bern, Switzerland.

Spogli L, Alfonsi L, Cilliers PJ, Correia E, De Franceschi G, Mitchell CN, Romano V, Kinrade J, Cabrera MA. 2013. GPS scintillations and total electron content climatology in the southern low, middle and high latitude regions. *Ann Geophys* **56(2)**: R0220. https://doi.org/10.4401/ag-6240.

Stolle C, Lühr H, Fejer BG. 2008. Relation between the occurrence rate of ESF and the equatorial vertical plasma drift velocity at sunset derived from global observations. *Ann Geophys* **26(12)**: 3979–3988. https://doi.org/10.1029/2005JA011330.

Su SY, Liu CH, Ho HH, Chao CK. 2006. Distribution characteristics of topside ionospheric density irregularities: Equatorial versus midlatitude regions. *J Geophys Res: Space Phys* **111(A6)**: A06305. https://doi.org/10.1029/2005JA011330.

van Dierendonck AJ, Arbesser-Rastburg B. 2004. Measuring Ionospheric scintillation in the equatorial region over Africa, including measurements from SBAS geostationary satellite signals. In: Proceedings of the ION GNSS 2004, Institute of Navigation, Long Beach, CA, September 21–24, 2004, pp. 316–324.

van Dierendonck AJ, Klobuchar J, Hua Q. 1993. Ionospheric scintillation monitoring using commercial single frequency C/A code receivers. In: Proceedings of the 6th International Technical Meeting of the Satellite Division of The Institute of Navigation (ION GPS 1993), Salt Lake City, UT, 22-24 September, pp. 1333–1342.

Wang Y, Zhang QH, Jayachandran PT, Moen J, Xing ZY, Chadwick R, Ma YZ, Ruohoniemi JM, Lester M. 2018. Experimental evidence on the dependence of the standard GPS phase scintillation index on the ionospheric plasma drift around noon sector of the polar ionosphere. *J Geophys Res Space Phys* **123(3)**: 2370–2378. https://doi.org/10.1002/2017JA024805.

Xiong C, Park J, Lühr H, Stolle C, Ma SY. 2010. Comparing plasma bubble occurrence rates at CHAMP and GRACE altitudes during high and low solar activity. *Ann Geophy* **28(9)**: 1647–1658. https://doi.org/10.5194/angeo-28-1647-2010.

Xiong C, Xu J, Stolle C, van den Ijssel J, Yin F, Kervalishvili GN, Zangerl F. 2020. On the occurrence of GPS signal amplitude degradation for receivers on board LEO satellites. *Space Weather* **18(2)**: e2019SW002398. https://doi.org/10.1029/2019SW002398.

Xiong C, Yin F, Luo X, Jin Y, Wan X. 2019. Plasma patches inside the polar cap and auroral oval: the impact on the spaceborne GPS receiver. *J Space Weather Space Clim* **9**: A25. https://doi.org/10.1051/swsc/2019028.

Xu DY, Morton Y, Yu J, Rino C. 2018. Simulation and tracking algorithm evaluation for scintillation signals on LEO satellites traveling inside the ionosphere. In: 2018 IEEE/ION position, location and navigation symposium (PLANS), Monterey, CA, April 23–26, 2018, pp. 1143–1149. https://doi.org/10.1109/PLANS.2018.8373498.

Yang Z, Liu Z. 2016. Correlation between ROTI and ionospheric scintillation indices using Hong Kong low-latitude GPS data. *GPS Solut* **20(4)**: 815–824. https://doi.org/10.1007/s10291-015-0492-y.

Yasyukevich YV, Yasyukevich AS, Astafyeva EI. 2021. How modernized and strengthened GPS signals enhance the system performance during solar radio bursts. *GPS Solut* **25**: 46. https://doi.org/10.1007/s10291-021-01091-5.

Yeh KC, Liu CH. 1982. Radio wave scintillations in the ionosphere. *Proc IEEE* **70(4)**: 324–360. https://doi.org/10.1109/proc.1982.12313.

Cite this article as: Zheng Y, Xiong C, Jin Y, Liu D, Oksavik K, et al. 2022. The refractive and diffractive contributions to GPS signal scintillation at high latitudes during the geomagnetic storm on 7–8 September 2017. *J. Space Weather Space Clim.* **12**, 40. https://doi.org/10.1051/swsc/2022036.